Order parameter free enhanced sampling of the vapor-liquid transition using the generalized replica exchange method

Qing Lu,[1] Jaegil Kim,[2,a)] and John E. Straub[2,b)]
[1]*Division of Materials Science and Engineering, Boston University, Brookline, Massachusetts 02446, USA*
[2]*Department of Chemistry, Boston University, Boston, Massachusetts 02215, USA*

(Received 8 January 2013; accepted 25 February 2013; published online 14 March 2013)

The generalized Replica Exchange Method (*g*REM) is extended into the isobaric-isothermal ensemble, and applied to simulate a vapor-liquid phase transition in Lennard-Jones fluids. Merging an optimally designed generalized ensemble sampling with replica exchange, *g*REM is particularly well suited for the effective simulation of first-order phase transitions characterized by "backbending" in the statistical temperature. While the metastable and unstable states in the vicinity of the first-order phase transition are masked by the enthalpy gap in temperature replica exchange method simulations, they are transformed into stable states through the parameterized effective sampling weights in *g*REM simulations, and join vapor and liquid phases with a succession of unimodal enthalpy distributions. The enhanced sampling across metastable and unstable states is achieved without the need to identify a "good" order parameter for biased sampling. We performed *g*REM simulations at various pressures below and near the critical pressure to examine the change in behavior of the vapor-liquid phase transition at different pressures. We observed a crossover from the first-order phase transition at low pressure, characterized by the backbending in the statistical temperature and the "kink" in the Gibbs free energy, to a continuous second-order phase transition near the critical pressure. The controlling mechanisms of nucleation and continuous phase transition are evident and the coexistence properties and phase diagram are found in agreement with literature results. © *2013 American Institute of Physics*. [http://dx.doi.org/10.1063/1.4794786]

I. INTRODUCTION

The replica exchange method (REM) (or parallel tempering)[1,2] has been widely used in the computer simulation of diverse complex systems such as proteins,[3–6] glasses,[8–10] and atomic clusters,[11,12] where methods based on sampling the conventional canonical ensemble struggle to attain ergodic sampling over a rugged energy landscape characterized by multiple minima separated by high barriers.[13–15] In the standard temperature REM (*t*REM), a set of statistically independent canonical molecular dynamics (MD) or Monte Carlo (MC) simulations run in parallel at specified temperatures. The coupling of low and high temperature replicas via exchanges of configurations allows the low temperature replicas to escape from trapped regions more easily, facilitating ergodic sampling.[12] While *t*REM has proven to be highly effective in the equilibrium sampling of stable phase states, the standard *t*REM struggles to attain its maximum power in the vicinity of a first-order phase transition.[16–20]

In moving across a strong phase change, canonical energy distributions are effectively disjointed and characterized by an energy gap corresponding to a latent heat. Since the acceptence probability of replica exchanges is determined by the energy overlap of neighboring replicas, an energy gap between $P_{T<T_c}(E)$ and $P_{T>T_c}(E)$ around the critical temperature T_c, $P_T(E)$ being the canonical probability density function (PDF) at the temperature T, significantly impairs replica exchanges. The acceptance of replica exchanges for a pair of inverse temperatures, β and β', close to $\beta_c = 1/T_c$, becomes exponentially suppressed as $A(\beta E;\beta' E') = \min[1, e^{\Delta\beta(E'-E)}] \approx e^{-|\Delta\beta\Delta E|}$, where $\Delta\beta = \beta' - \beta$ and ΔE is the energy gap. The generalized Replica Exchange Method (*g*REM)[21] has been developed to restore the full power of replica exchange by incorporating noncanonical ensembles into the replica exchange paradigm. The generalized ensemble sampling weights are determined from tailored effective temperatures through an inverse mapping strategy.

Illustrative simulations on a Potts spin system with varying system size and simulation conditions demonstrated a comprehensive sampling.[21] The quantitative comparison between *g*REM and Wang-Laudau (WL) sampling revealed that *g*REM provided an order of magnitude acceleration of tunneling transitions over WL, while maintaining a faithful sampling for the phase transition region as in flat histogram methods.

Application to the study of an adapted Dzutugov model explored the effectiveness of *g*REM in sampling a solid-liquid phase transition.[22] In this work, *g*REM is used to study the vapor-liquid phase transition in Lennard-Jones fluids, which has been the subject of extensive studies.[23–28]

Originally, *g*REM was formulated at constant volume where the internal energy of the system was a natural dynamical variable. However, in most vapor-liquid transition experiments the pressure, or, equivalently, the chemical potential of

a)Present address: Broad Institute of MIT and Harvard, Cambridge, Massachusetts 02142, USA.
b)Author to whom correspondence should be addressed. Electronic mail: straub@bu.edu.

the vapor, is held constant.[29–31] Approaches informed by classical nucleation theory (CNT) usually consider the formation and growth of a liquid droplet at constant pressure.[32–34] In this work, *g*REM is extended to include volume fluctuation at constant pressure for the effective simulation of the vapor-liquid transitions.

In a standard NPT ensemble, the liquid cluster cannot coexist stably in the vapor phase. The liquid cluster that is bigger than the critical size will grow in order to minimize the excess free energy, while the cluster that is smaller than the critical size will shrink, in order to lower the excess free energy. Ten Wolde and Frenkel[29,35] used a biased Monte Carlo ("umbrella sampling") approach to stabilize large droplets. Schrader, Virnau, and Binder[36] used the successive umbrella sampling to observe the liquid droplets coexisting in stable thermal equilibrium with supersaturated vapor at a range of densities. While these methods are successful in probing metastable states associated with the liquid-vapor transition, they rely on the identification of a "good" order parameter for the transition, to exploit in the application of biased sampling, which can be difficult to identify in more complex systems.[7]

The *g*REM approach allows an effective sampling of metastable and unstable states in the vapor-liquid coexistence states, independent of knowledge of an effective order parameter for the transition. In a *g*REM simulation, each stage of the phase transition can be stabilized, including the formation of a liquid droplet, the growth of a liquid cluster, and vanishing of the vapor phase. Recently, a crossover from a purely nucleation-controlled process to a spinodal decomposition was predicted for LJ fluids in a deeply supercooled regime.[37,38] Since we are able to observe the whole transition process through *g*REM simulation, we can effectively assess the mechanism of the vapor-liquid phase transition at various conditions.

The paper is organized as follows. In Sec. II, the methodology is described and in Sec. III, we compare the sampling effectiveness of *g*REM with *t*REM approaches, and present simulation results of phase behavior, including the phase diagram, the Gibbs free energy as a function of pressure, and the structural properties at low and high pressures. Salient conclusions are presented in Sec. IV.

II. METHODS AND MATERIALS

A. Generalized replica exchange method at constant pressure

Originally, *g*REM was formulated at constant volume, where the internal energy E of the system is a natural variable at the fixed volume V. To incorporate volume fluctuation critical to a vapor-liquid transition, we extended *g*REM to the isothermal-isobaric—NPT ensemble.[22] The enthalpy, $H = E + PV$, which describes the thermal energy change when a process occurs at a constant pressure, P, becomes a key dynamical variable in the NPT ensemble. The density of states in enthalpy is defined as $\Omega(H;P) = \int dV \int d^3r \delta[H(E(r),V) - (E+PV)]$. The isobaric entropy is $S(H;P) = k_B \ln\Omega(H;P)$ ($k_B = 1$), analogous to the entropy in the microcanonical ensemble, and the statistical temperature is $T_S(H) = [\partial S/\partial H]^{-1}$.

Each replica α in *g*REM simulation with M replicas ($\alpha = 1, \ldots, M$) is associated with an effective temperature $T_\alpha(H;\lambda_\alpha)$, and sampled with generalized ensemble weight $W(H;\lambda_\alpha)$. The sampling weight $W_\alpha(H,\lambda_\alpha)$ is determined from the effective temperature through the inverse mapping strategy as

$$W_\alpha(H) = -\ln \int \frac{1}{T_\alpha(H';\lambda_\alpha)} dH'. \tag{1}$$

The linear effective temperatures are aligned in parallel as

$$T_\alpha(H;\lambda_\alpha) = \lambda_\alpha + \gamma(H - H_0) \tag{2}$$

with the control parameters including γ, the constant slope, H_0, a constant in the relevant enthalpy range, and λ_α, the T-intercept at a chosen H_0. Denoting the lowest and highest temperature as T_1 and T_M, respectively, the average enthalpy $\tilde{H}_1$ and $\tilde{H}_M$ can be determined by short canonical runs at T_1 and T_M. The value of H_0 can be set as $H_0 = \tilde{H}_1$. The dynamic range of λ_α is determined as $\lambda_1 = T_1$ and $\lambda_M = T_M - \gamma(\tilde{H}_M - \tilde{H}_1)$, so that the first and Mth effective temperatures cross $[\tilde{H}_1, T_1]$ and $[\tilde{H}_M, T_M]$, respectively. The intermediate values of λ_α ($1 < \alpha < M$) are determined by equally dividing the parameter space as

$$\lambda_\alpha = \lambda_1 + (\alpha - 1)\Delta\lambda \tag{3}$$

and $\Delta\lambda = (\lambda_M - \lambda_1)/(M-1)$.

Detailed simulation protocols of *g*REM are defined by the following three steps:

(i) Perform short canonical runs at several temperatures between T_1 and T_M to determine the data set, $[\tilde{H}_\alpha, T_\alpha]$. Select a proper γ to be less than the minimum slope of the statistical temperature T_S, and determine λ_α by employing Eq. (3) between $\lambda_1 = T_1$ and $\lambda_M = T_M - \gamma(\tilde{H}_M - \tilde{H}_1)$, with $H_0 = \tilde{H}_1$.

(ii) Run the *g*REM simulation in each replica by making Monte Carlo trial moves in configuration space with the acceptance probability

$$A_{\text{intra}}(\mathbf{x} \to \mathbf{x}') = \min[1, e^{w_\alpha(H) - w_\alpha(H')}], \tag{4}$$

where the effective potential $w_\alpha(H) = -\ln W_\alpha$, W_α being the sampling weight.

A Monte Carlo trial move consists either of an attempted single particle displacements or a trial volume change; one trial volume move is made after N trial single particle displacements are performed, where N equals the number of particles.

After all replicas finished N attempted single particle displacement and a trial volume move, attempt a replica exchange between neighboring replicas with the acceptance

$$A_{\text{inter}}(\alpha;\mathbf{x}\mathbf{x}') = \min[1, \exp(\Delta_\alpha)], \tag{5}$$

$\Delta_\alpha = w_{\alpha+1}(H') - w_{\alpha+1}(H) + w_\alpha(H) - w_\alpha(H')$, where $H = E(r) + PV$ and $H' = E(r') + PV'$.

(iii) Once a sufficiently long production run has been performed, calculate the entropy estimate $\tilde{S}(H)$ by joining multiple generalized ensemble runs via the weighted

histogram analysis method (WHAM)[39] or statistical temperature weighted histogram analysis method (ST-WHAM).[40]

B. Statistical temperature weighted histogram analysis method (ST-WHAM)

A recently developed statistical temperature weighted histogram analysis method (ST-WHAM)[40] is used for posterior analysis of *g*REM simulation results. This method takes advantage of the already-determined sampling weights of replica, $W_\alpha(H)$, and the associated enthalpy histogram, $\mathrm{P}_\alpha(H)$, where P denotes the histogram and H denotes the enthalpy. The goal is to directly determine the inverse statistical temperature $\beta_S = \partial S/\partial H$ as a weighted superposition of the individual statistical temperature estimates, without undetermined parameters. Thermodynamic quantities such as entropy can be evaluated upon the numerical integration of this statistical temperature. Unlike conventional WHAM,[39] ST-WHAM does not use the iterative technique to determine the relevant partition function, but instead determines β_S directly from $W_\alpha(H)$ and $\mathrm{P}_\alpha(H)$. This leads to a substantial acceleration of the data analysis without a loss in accuracy as has been demonstrated in a number of recent applications.[41,42] A more complete description of ST-WHAM is provided in the supplementary material.[53]

C. Lennard-Jones fluid

We study the vapor-liquid phase transition in a Lennard-Jones system[43] in which the interaction potential was truncated and shifted at a cutoff radius $r_c = 2.5\sigma$, where σ is the particle diameter. The energy of interaction φ between any two particles separated by a distance r is given by

$$\varphi(r) = \begin{cases} \varphi_{\mathrm{LJ}}(r) - \varphi_{\mathrm{LJ}}(r_c) & r < r_c \\ 0 & r \geq r_c, \end{cases}$$

where $\varphi_{\mathrm{LJ}}(r) = 4\epsilon(\sigma^{12}/r^{12} - \sigma^6/r^6)$ is the full LJ interaction, ϵ and σ are the LJ well depth and diameter, and $r_c = 2.5\sigma$ is the interaction cutoff separation. We made no long-range corrections and applied cubic periodic boundary conditions. Reduced units employ ϵ and σ as characteristic energy and length scales, respectively. The numerical values for argon are $\sigma = 0.3405$ nm, $\epsilon_k = 119.8$ K.

III. RESULTS AND DISCUSSION

A. Sampling effectiveness

A comparative study was performed between *g*REM and *t*REM simulations in order to explore the difference in sampling effectiveness. The simulations were performed at pressure $P = 0.04$ for a system with 250 particles, and number of replicas $M = 99$ in both *t*REM and *g*REM simulations. For *t*REM, the temperature of each replica was equally allocated between the lowest and highest temperature $T_1 = 0.7$ and $T_M = 1.1$. The effective temperature of *g*REM simulation obeys Eq. (2), and the parameters in the effective temperature are $H_0 = -1218.6$, $\lambda_1 = 0.7$, $\lambda_M = 5.1$ and $\gamma_0 = -0.0029046$.

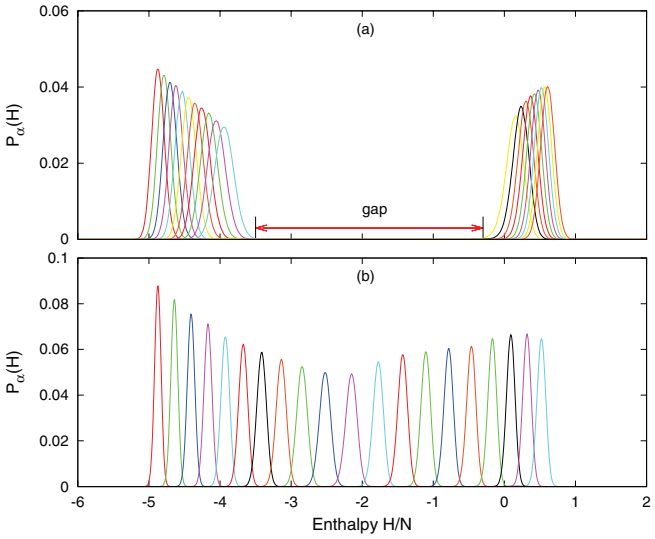

FIG. 1. (a) and (b) show the resulting generalized probability distribution functions (GPDF) of replica 1,6,11,16,⋯,96 sampled by *t*REM and *g*REM, respectively. The enthalpy gap in *t*REM is marked in (a).

In the strong first order phase transition, the statistical temperature $T_S(H)$ exhibits a negative slope, the so-called backbending or S-loop. Instead of using canonical temperatures, *g*REM uses effective temperatures in order to form unique stable crossing points with the statistical temperature, T_S. The linear effective temperatures of different replicas, T_α, are aligned in parallel with a constant slope γ, which is less than the slope of T_S in the backbending region. As a result, unique crossing points are formed between T_α and T_S throughout the enthalpy range of interest. An illustration of linear effective temperature is provided in the supplementary material.[53]

Since $T_\alpha(H; \lambda_\alpha)$ was designed to form a unique, stable crossing point, H^*_α, with $T_S(H)$, the resulting PDFs are sharply localized around H^*_α with a Gaussian shape in Fig. 1(b), and naturally bridge the vapor and liquid phases with unimodal enthalpy distributions across the transition region. In contrast, the canonical enthalpy distributions of *t*REM are effectively disjoint by an enthalpy gap corresponding to the latent heat between vapor and liquid phases, which is displayed in PDFs in Fig. 1(a). Note that only 20 out of 99 replicas were plotted in Fig. 1 and actual overlaps between neighboring replicas are greater.

During the simulations, we kept track the movement of replicas of both *t*REM and *g*REM in the enthalpy space. Figure 2 shows the trajectories of replica 61 and 14 of both *t*REM and *g*REM. While the *t*REM trajectories sample two narrow ranges in enthalpy space, the trajectories of *g*REM reach the lowest and highest boundaries and span the enthalpy space. The tunneling transitions[44] in the two replicas and other replicas (not shown) enable the mixing between the high and low enthalpy configurations. The *g*REM simulation achieves comprehensive sampling in the phase transition region, while *t*REM fails because of the intrinsic instability of canonical ensemble in the backbending region.

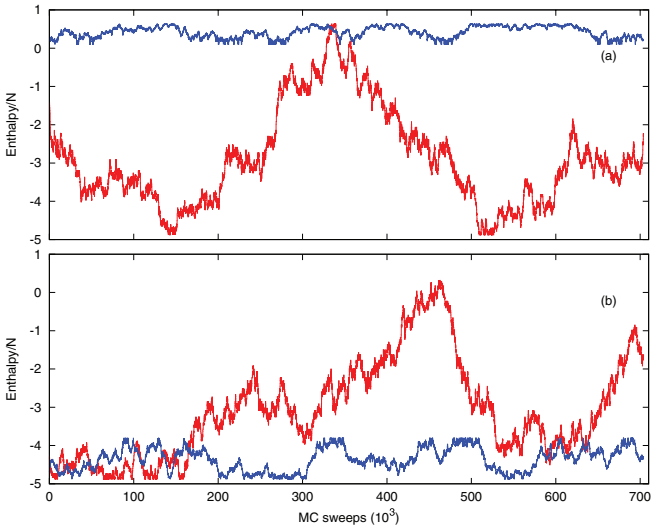

FIG. 2. (a) The enthalpy trajectories of replica 14 in *t*REM (blue line) and *g*REM (red line). (b) The enthalpy trajectories of replica 61 in *t*REM (blue line) and *g*REM (red line).

B. Vapor-liquid phase coexistence properties and phase diagram

*g*REM simulations were carried out for systems at seven pressures and with two different sizes, 250 and 1000 particles, exploring temperatures as functions of enthalpy and density, $T(H)$ and $T(\rho)$, and liquid-vapor coexistence points and spinodal points at each pressure.

The line of equilibrium coexistence of two phases in a one-component system corresponds to equalities of the pressures, temperatures, and the chemical potentials of the liquid and vapor phases. At equilibrium, the Gibbs free energy difference, $\Delta G = (H_{\rm vap} - H_{\rm liq}) - T\int_{\rm liq}^{\rm vap} dS = 0$, $H_{\rm vap}$ and $H_{\rm liq}$ being the enthalpy of vapor and liquid phases at the coexistence temperature. Given that the statistical temperature $T_S(H) = (\partial H/\partial S)_{N,P}$, integration yields $\Delta S = \int_{H_{\rm liq}}^{H_{\rm vap}} dH/T_S(H)$. Therefore, the coexistence temperature must satisfy

$$\frac{\Delta G}{T} = \frac{H_{vap} - H_{liq}}{T} - \int_{H_{liq}}^{H_{vap}} \frac{dH}{T_S(H)} = 0. \qquad (6)$$

Equation (6) is equivalent to the Maxwell equal area rule. The equilibrium temperatures on the coexistence curve are determined through this method.

For the simulations of $N = 1000$ and $N = 250$ systems, 99 replicas are used, and the other parameters are in the supplementary material.[53] The critical temperature, T_c, and density, ρ_c, can be obtained through fitting the coexistence points to Guggenheim-type equations.[47,48] For $N = 250$ system, $T_c = 1.0780$ and $\rho_c = 0.3198$ and for $N = 1000$ system, $T_c = 1.0730$ and $\rho_c = 0.3224$. Vrabec *et al.* reported similar values as $T_c = 1.0779$ and $\rho_c = 0.3190$. The coexistence and critical points of these three systems are shown in Fig. 3.

While crossing the phase coexistence of binodal curve, the system enters the metastable phase, which retains its restorative reaction to small perturbations of density.[24]

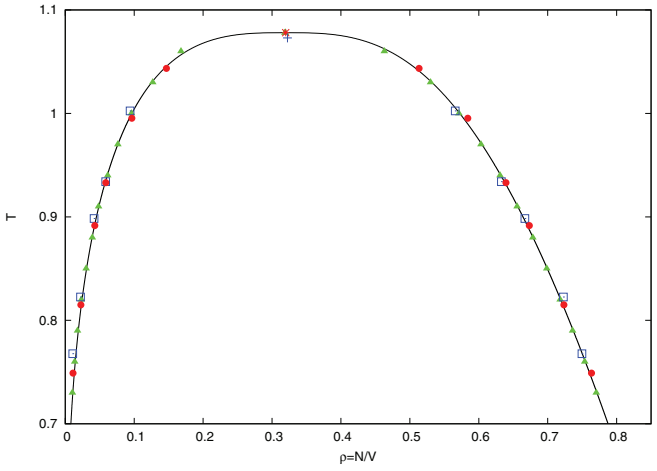

FIG. 3. The coexistence temperatures and densities of the $N = 250$ system are plotted with red filled circles, and that of the $N = 1000$ system is plotted as blue squares. The critical temperature and density for $N = 250$ and $N = 1000$ system is denoted by the red star and blue cross, respectively. The error bars for the present simulations are smaller than the figure symbols. The critical and coexistence points reported by Vrabec *et al.*[47] are in green filled triangles.

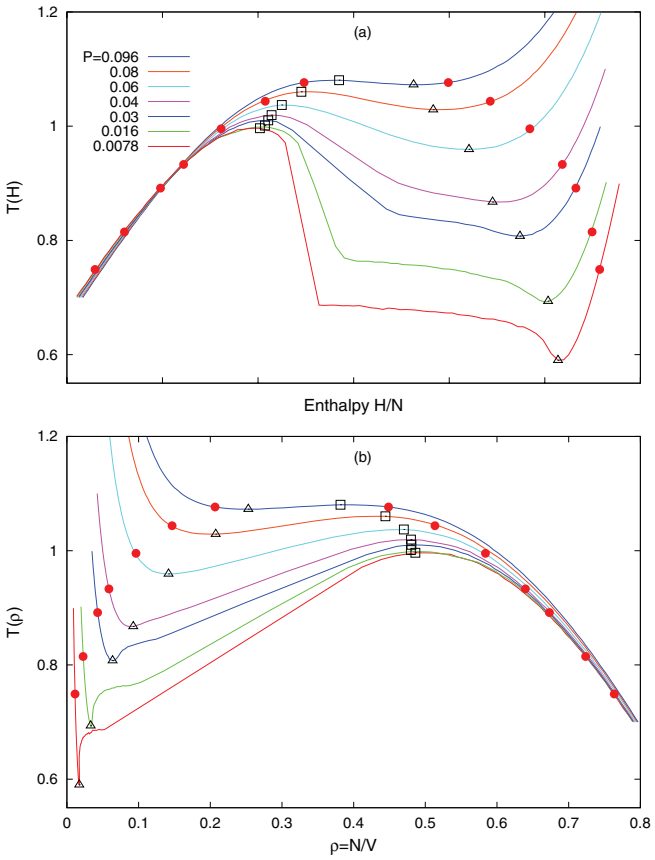

FIG. 4. (a) Temperatures $T(H)$ as functions of enthalpy at seven different pressures for systems with 250 particles. The liquid-vapor coexistence temperature and enthalpy points (T_{CE}, H_{CE}) are plotted as red filled circles. The black open squares and triangles denote liquid and vapor spinodal points, respectively. (b) Temperatures $T(\rho)$ as functions of density at seven different pressures. Same colors and symbols are used for the same simulations in both (a) and (b).

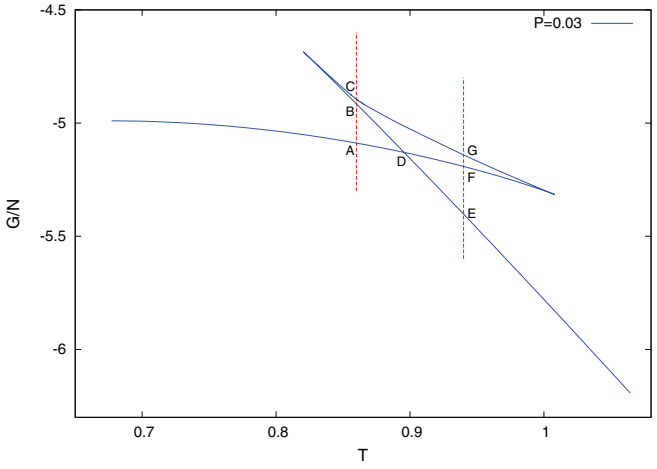

FIG. 5. The temperature variation of Gibbs free energy per particle, $G(T)/N$, at pressure $P = 0.03$. The letters $A - G$ denote the states on the Gibbs function.

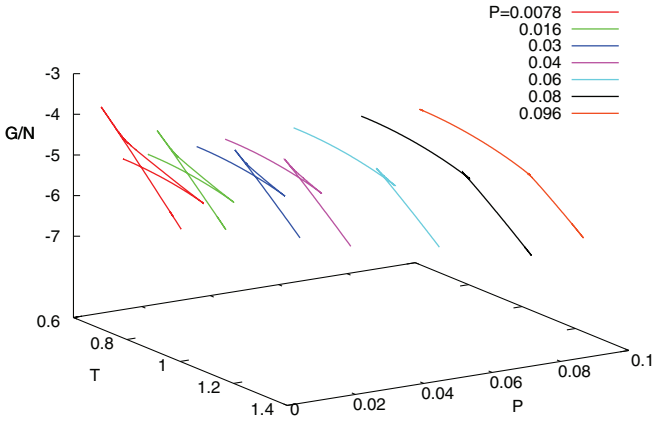

FIG. 6. Behavior of the Gibbs free energy per particle, $G(T)/N$, as a function of temperature at seven different pressures.

Conditions of stability against this kind of perturbation are violated only when the system reaches the spinodal, which is the locus of points surrounding the unstable region.[45] The spinodal points can be simply identified by the maximum and minimum of the $T(H)$ and $T(\rho)$ curves as shown in Figs. 4(a) and 4(b). The density region bounded by spinodal points has a positive slope, giving a negative thermal expansion coefficient and indicating an instability.

The degree of backbending in the $T(H)$ curve gradually decreases as the pressure increases. At some low pressures, such as $P1 = 0.0078$, the transition region of $T(H)$ displays severe backbending. When pressure reaches $P7 = 0.096$, which is close to the critical pressure,[46] the backbending is almost transformed into an inflection and the first order phase transition becomes second-order, in agreement with the theoretical prediction for the behavior at the critical point.

C. Thermodynamic properties calculated from ST-WHAM

We employed ST-WHAM to compute the entropy and subsequently the Gibbs free energy for the system of 1000 particles. The temperature variation of Gibbs free energy per particle, $G(T)/N$, at pressure $P = 0.03$ is shown in Fig. 5. The Gibbs function intersects itself at point D, which is the liquid-vapor coexistence point and the liquid and vapor phases are the sections on the left and right sides of point D, respectively. The liquid and vapor curves are connected together through the intermediate states on the kink where the curvature changes sign. Following Callen,[49] we refer to the kink on the Gibbs function as the closed loop. The discontinuity of the curvatures of liquid and vapor curves is the characteristic of a first order phase transition.

The closed loop results from the fact that enthalpy function, $H(T)$, is triple-valued in T for the backbending regime. For a given temperature, three states are available to the system, as, for example, the states designated by A, B, and C. Among these three states, state C is unstable to small

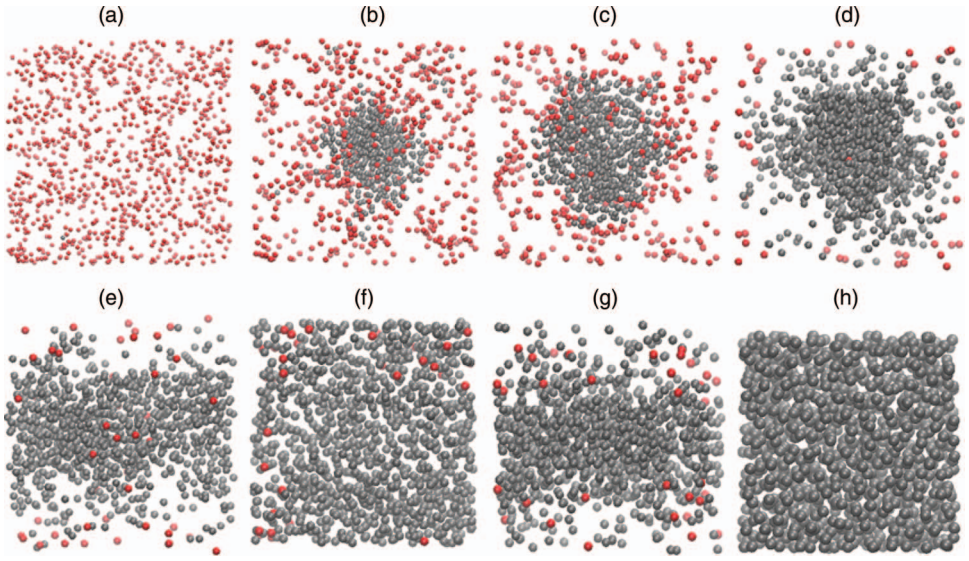

FIG. 7. Configurations of 6 different states throughout the phase transition at $P3 = 0.03$. The vapor particles are in red and the liquid particles are in gray. (e) and (g) are side views of the states in (d) and (f), respectively. Note that the size of each box is not proportional to the volume of the state.

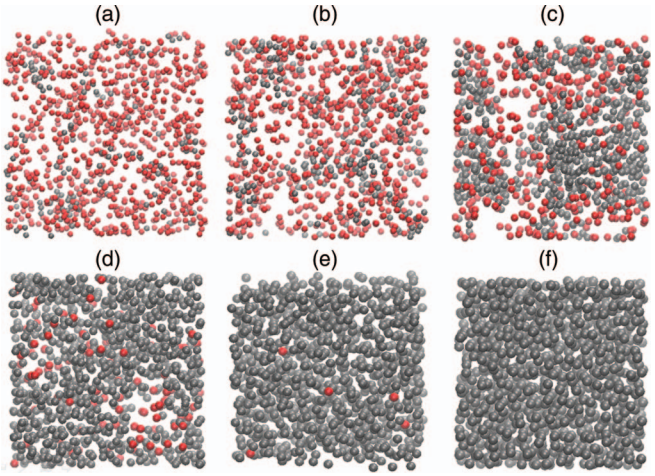

FIG. 8. Configuration of 6 different states throughout the phase transition at $P7 = 0.096$. The color scheme is the same as in Fig. 7. Note that the size of each box is not proportional to the volume of the state.

fluctuations in density. A and B are stable, and the Gibbs function is a local minimum. In generalized ensemble sampling, such as gREM simulation, the metastable and unstable states such as state B and C are transformed into stable states. Similarly, the Gibbs function is tripled-valued at another temperature, where states E, F, and G, are stable, metastable, and unstable states, respectively, in the canonical ensemble.

We have shown that backbending in $T(H)$ curves decreases with the increasing pressure in Fig. 4. Because the closed loop in $G(T)/N$ curves are the result of the backbending in $T(H)$, we expect the closed loop will shrink when the pressure increases. Figure 6 presents the evolution of the Gibbs function at seven different pressures. The closed loop is large at the low pressures, becomes smaller with the increasing pressure, and at $P = 0.096$ the closed loop almost disappears. With the diminishment of the closed loop, the Gibbs functions of the liquid and vapor phases are connected together without the discontinuity in the curvatures, and the liquid-vapor phase transition becomes a second order continuous phase transition.

D. Structural properties

It is known that nucleation and continuous phase transition are the two mechanisms that control the first-order and second-order phase transitions, respectively. Direct inspection of the atomic configurations will validate the statement. The configurations of the system at a lower pressure, $P3 = 0.03$, and near the critical pressure, $P7 = 0.096$, are shown in Figs. 7 and 8, respectively. The vapor particles are marked in red and the liquid particles are in gray. Stillinger's criterion[50] was used to determine whether a particle is liquid-like or vapor-like, and the cutoff radius is $r_c = 1.5$. The results presented in this section are for systems with 1000 particles.

The configurations of six states, denoted as states 1 to 6, are shown in Fig. 7. Beginning with the pure vapor phase in state 1, a spherical liquid droplet is seen in state 2, the spherical droplet grows larger in state 3, becomes cylinder-like in state 4, grows into a slab-like shape in state 5, and in state 6 reaches the pure liquid phase. The occurrence of these states agrees with results in previous work.[36,51,52] The structural change of the states along the transition path shows that nucleation is the controlling mechanism of the vapor-liquid phase transition at $P3$.

The configurations of the system at $P7 = 0.096$ are shown in Fig. 8. From Fig. 8(a) to 8(f), the system gradually transforms from vapor to liquid phase but stays homogenous without the phase domain separation. At this pressure, the growth of liquid phase takes place in a collective and diffusive manner.

IV. CONCLUSION

In this work, we demonstrated the advantages of gREM in simulating the vapor-liquid phase transition in the truncated and shifted Lennard-Jones fluid. The parameterized effective temperatures in gREM are tailored to avoid an intrinsic instability of the canonical ensemble in the negative slope region of the statistical temperature $T_S(H)$ in first order phase transition. The optimal sampling weight is determined from the effective temperature through the inverse mapping strategy. By combining generalized ensemble sampling with replica exchange, our method enables a comprehensive sampling for phase transition region with a succession of unimodal enthalpy distributions.

Originally formulated in NVT ensemble, gREM has been extended to the isothermal-isobaric (NPT) ensemble to accommodate the volume change in vapor-liquid phase transition. The phase transition was studied at various pressures below and close to the critical point. The statistical temperature as a function of enthalpy $T_S(H; P)$ is computed at each pressure by ST-WHAM based on the data produced by gREM simulations. The coexistence temperatures and densities are calculated through the Maxwell equal area construction. The spinodal points are identified as the maximum and minimum points of the $T_S(H)$ curves. Our results are consistent with the literature[47] results.

We studied the change in the nature of liquid-vapor phase transition with the change in the pressure. At low pressures, strong first-order phase transition features are observed as the backbending in the statistical temperature as a function of enthalpy, $T_s(H)$, and the closed loop in Gibbs function, $G(T)$. However, as the pressure increases, the first-order features gradually diminishes, and the liquid and vapor phases are connected together without discontinuity in the curvature of enthalpy and Gibbs function. The diminishment of the discontinuity indicates that the liquid-vapor transition becomes second-order continuous phase transition near the critical pressure.

Direct inspection of the atomic configurations of the intermediate states has shown the controlling mechanisms in the two scenarios. At low pressures, it is apparent that nucleation controls the vapor-liquid phase transition as shown by the liquid droplet formation and growth process. Near the critical pressure, a coalescence or collective growth of the new phase displays the characteristic of a second order phase transition.

The comprehensive sampling for metastable or unstable states with no additional order parameters, explicitly demonstrated in vapor-liquid phase transition of Lennard-Jones fluids, makes *g*REM a promising tool in diverse applications of complex fluids, water and protein simulations.

ACKNOWLEDGMENTS

We are grateful to the National Science Foundation (Grant No. CHE-1114676) for the generous support of our research.

[1]C. J. Geyer and A. Thompson, J. Am. Stat. Assoc. **90**, 909 (1995).
[2]K. Hukushima and K. Nemoto, J. Phys. Sco. Jpn. **65**, 1604 (1996).
[3]Y. Sugita and Y. Okamoto, Chem. Phys. Lett. **314**, 141 (1999).
[4]R. Zhou and B. J. Berne, Proc. Natl. Acad. Sci. U.S.A. **99**, 12777 (2002).
[5]A. E. Garcia and J. N. Onuchic, Proc. Natl. Acad. Sci. U.S.A. **100**, 13898 (2003).
[6]U. H. E. Hansmann, Chem. Phys. Lett. **281**, 140 (1997).
[7]T. B. Woolf, D. M. Zuckerman, N. Lu, and H. Jang, J. Mol. Graphics Modell. **22**, 359 (2004).
[8]R. Yamamoto and W. Kob, Phys. Rev. E **61**, 5473 (2000).
[9]E. Flenner and G. Szamel, Phys. Rev. E **73**, 061505 (2006).
[10]B. A. Berg and T. Celik, Phys. Rev. Lett. **69**, 2292 (1992).
[11]P. A. Frantsuzov and V. A. Mandelshtam, Phys. Rev. E **72**, 037102 (2005).
[12]P. Poulain, F. Calvo, R. Antoine, M. Broyer, and P. Dugourd, Phys. Rev. E **73**, 056704 (2006).
[13]H. Li, G. Li, B. A. Berg, and W. Yang, J. Chem. Phys. **125**, 144902 (2006).
[14]A. Mitsutake, Y. Sugita, and Y. Okamoto, Biopolymers **60**, 96 (2001).
[15]B. J. Berne and J. E. Straub, Curr. Opin. Struct. Biol. **7**, 181 (1997).
[16]D. J. Earl and M. W. Deem, Phys. Chem. Chem. Phys. **7**, 3910 (2005).
[17]H. Kamberaj and A. van der Vaart, J. Chem. Phys. **127**, 234102 (2007).
[18]C. Zhang and J. Ma, Phys. Rev. E **76**, 036708 (2007).
[19]E. Lyman, F. M. Ytreberg, and D. M. Zuckerman, Phys. Rev. Lett. **96**, 028105 (2006).
[20]M. R. Shirts and J. D. Chodera, J. Chem. Phys. **129**, 124105 (2008).
[21]J. Kim, T. Keyes, and J. E. Straub, J. Chem. Phys. **132**, 224107 (2010).
[22]Q. Lu, J. Kim, and J. Straub, J. Phys. Chem. B **116**, 8654 (2012).
[23]B. Smit, J. Chem. Phys. **96**, 8639 (1992).
[24]V. G. Baidakov, S. P. Protsenko, Z. R. Kozlova, and G. G. Chernykh, J. Chem. Phys. **126**, 214505 (2007).
[25]X. C. Zeng and D. W. Oxtoby, J. Chem. Phys. **94**, 4472 (1991).
[26]J. R. Errington, J. Chem. Phys. **118**, 9915 (2003).
[27]A. R. Imre, G. Mayer, G. Hazi, R. Rozas, and T. Kraska, J. Chem. Phys. **128**, 114708 (2008).
[28]V. V. Brazhkin, Y. D. Fomin, A. G. Lyapin, V. N. Ryzhov, and E. N. Tsiok, J. Phys. Chem. B **115**, 14112 (2011).
[29]P. R. ten Wolde and D. Frenkel, J. Chem. Phys. **109**, 9901 (1998).
[30]M. P. Allen and D. J. Tildesley, *Computer Simulation of Liquids* (Clarendon, 1987).
[31]D. Frenkel and B. Smit, *Understanding Molecular Simulation: From Algorithms to Applications* (Academic, 1996).
[32]J. Frenkel, *Kinetic Theory of Liquids* (Dover, 1955).
[33]F. F. Abraham, *Homogeneous Nucleation Theory* (Academic, 1974).
[34]K. Binder and D. Stauffer, Adv. Phys. **25**, 343 (1976).
[35]P. R. ten Wolde, M. J. Ruiz-Montero, and D. Frenkel, J. Chem. Phys. **110**, 1591 (1999).
[36]M. Schrader, P. Virnau, and K. Binder, Phys. Rev. E **79**, 061104 (2009).
[37]P. Bhimalapuram, S. Chakrabarty, and B. Bagchi, Phys. Rev. Lett. **98**, 206104 (2007).
[38]J. Wedekind, G. Chkonia, J. Wolk, R. Strey, and D. Reguera, J. Chem. Phys. **131**, 114506 (2009).
[39]A. M. Ferrenberg and R. H. Swenden, Phys. Rev. Lett. **63**, 1195 (1989).
[40]J. Kim, T. Keyes, and J. E. Straub, J. Chem. Phys. **135**, 061103 (2011).
[41]L. G. Rizzi and N. A. Alves, J. Chem. Phys. **135**, 141101 (2011).
[42]M. Church, C. Ferry, and A. E. van Giessen, J. Chem. Phys. **136**, 245102 (2012).
[43]J. E. Lennard-Jones, Proc. R. Soc. London, Ser. A **106**, 441 (1924).
[44]S. Trebst, M. Troyer, and U. H. E. Hansmann, J. Chem. Phys. **124**, 174903 (2006).
[45]D. Chandler, *Introduction to Modern Statistical Mechanics* (Oxford University Press, New York, 1987).
[46]H. S. Ashbaugh, J. Chem. Phys. **130**, 204517 (2009).
[47]J. Vrabec, G. K. Kedia, G. Fuchs, and H. Hasse, Mol. Phys. **104**, 1509 (2006).
[48]E. A. Guggenheim, J. Chem. Phys. **13**, 253 (1945).
[49]H. B. Callen, *Thermodynamics: An Introduction to the Physical Theories of Equilibrium Thermostatics and Irreversible Thermodynamics* (Wiley, 1985).
[50]F. H. Stillinger, J. Chem. Phys. **38**, 1486 (1963).
[51]L. G. MacDowell, V. K. Shen, and J. R. Errington, J. Chem. Phys. **125**, 034705 (2006).
[52]R. Godawat, S. N. Jamadagni, J. R. Errington, and S. Garde, Ind. Eng. Chem. Res. **47**, 3582 (2008).
[53]See supplementary material at http://dx.doi.org/10.1063/1.4794786 for the detailed description of ST-WHAM, a figure on linear effective temperature, and tables for parameters in *g*REM simulations.